

# Residual Stress in Additive Manufactured Nickel Alloy 625 Parts

**Lindsey Bass**

National Institute of Standards and Technology,  
Gaithersburg, MD 20899  
e-mail: lindsey.bass@vt.edu

**Justin Milner**

National Institute of Standards and Technology,  
Gaithersburg, MD 20899  
e-mail: justin.milner@nist.gov

**Thomas Gnäupel-Herold**

National Institute of Standards and Technology,  
Gaithersburg, MD 20899  
e-mail: thomas.gnaeupel-herold@nist.gov

**Shawn Moylan**

National Institute of Standards and Technology,  
Gaithersburg, MD 20899  
e-mail: shawn.moylan@nist.gov

*One of the key barriers to widespread adoption of additive manufacturing (AM) for metal parts is the build-up of residual stresses. In the laser-based powder bed fusion process, a laser selectively fuses metal powder layer by layer, generating significant temperature gradients that cause residual stress within the part. This can lead to parts exceeding tolerances and experiencing severe deformations. In order to develop strategies to reduce the adverse effects of these stresses, the stresses first need to be quantified. Cylindrical Nickel Alloy 625 samples were designed with varied outer diameters, inner diameters, and heights. Neutron diffraction was used to characterize the three-dimensional (3D) stress state throughout the parts. The stress state of the parts was generally comprised of tensile exteriors and compressive interiors. Regardless of part height, only the topmost scan height of each part experienced large reductions in axial and hoop stress. Improved understanding of the residual stress trends will aid in model development and validation leading to techniques to reduce negative effects of the residual stress.*

[DOI: 10.1115/1.4039063]

## 1 Introduction

While additive manufacturing (AM) has increased in popularity for efficiently manufacturing customizable parts through the layer-by-layer fabrication approach, a potential for the build-up of residual stress in metal parts limits design capabilities and product robustness. Residual stress refers to extraneous stress left in parts when they are in equilibrium with their environment, which can be at the macro, micro (intergranular), and atomic level [1]. Shot-peened materials utilize induced compressive surface residual stress to improve fatigue resistance, and thermally toughened materials use induced residual stress to improve static loading [1]. However, most residual stress leads to unwanted cracks, deformation, or unexpected failure commonly in the form of layer delamination [2], warping, or lost part tolerances for AM parts [3]. This study explores what stresses are present in a simple part geometry and how geometric changes affect the three-dimensional (3D) residual stress state within the part. Measured residual stress will also be used to improve multiphysics models and simulations of AM processes, which will enhance the development of methods for reducing undesirable residual stress.

**1.1 Causes of Residual Stress.** The temperature gradient mechanism, inherent in the laser-based powder bed fusion process, illustrates one of the main causes of residual stress [4]. During this mechanism, the laser beam selectively fuses metal powder causing a steep temperature gradient. This causes local expansion in the melt pool region resulting in compression of the material adjacent to the melt pool. Then, cooling creates a rapid shrinking resulting in tension. Process variables known to influence residual stress include laser speed, power, and energy density [5–9], laser focal diameter [7], melt pool size and shape [3,10], deposition speed [5], deposition or scan strategy [2,6–8,11–15], the presence of or cracks within a support structure [7,16], and postprocessing [4]. Material properties [1,17,18], texture [19], microstructure [3,8,20–27], part misfits [21], and part geometry [7,9] are additionally shown to affect residual stress.

**1.2 Prior Findings in Residual Stress Trends.** Parts are frequently comprised of tensile exterior stresses and compressive interior stresses with tension also occasionally forming at the base of the part [4–7,12,19,22,24,28]. On the other hand, some studies found the opposite trend along the vertical direction [19,20,28]. Higher residual stresses were generally found at the surface layer [4,5,7,18,29,30], along the deposition line or scanning direction [2,10,31–33], in parts left on the build plate [4,32], and with continuous scanning [14]. Very thick or very thin parts tended to have lower residual stress: while the many scan passes on thick parts could act like heat treatment, thin specimens exhibited low strength [30], which likely allowed for stress-relieving deformation. Material properties including yield strength and thermal expansion coefficient increased residual stress while porosity lowered it [4,5,22,31,34]. There were also some conflicts among conclusions. One study found highest stresses perpendicular to the scan direction [4], and another study found these stresses to be the lowest [34]. The spiral-in deposition pattern led to highest stresses in two studies [11,15] and the lowest stresses in one study [2]. Attributed to the fundamental differences arising from unique AM processes, materials, part geometries, and build parameters, these inconsistencies demonstrate the need for better understanding these factors when assessing residual stress in metal AM products since altering one factor could produce a completely different trend.

**1.3 Modeling Residual Stress.** The expansion of stress-modeling techniques continues to advance AM capabilities by simulating expected trends in residual stress, which could allow someone to modify regions of a part with stresses detrimental to its integrity prior to part fabrication. Many previous studies have obtained decent agreement between models and experimental data. Accurate residual stress models were found to be greatly dependent on factors including thermal gradients, exposure strategy, layer thickness, or laser power [4,6,12,35–38]. Two-dimensional (2D) stress fields have been mapped [10], and the process map approach presents a 3D layout depicting relationships among three distinct variables influencing residual stress [3,5]. Many studies have applied thermal or thermomechanical modeling approaches to analyze temperature or stress distributions [11,15,17,36,39–45]. Other models have targeted deflection measurements for different deposition parameters [2,13], and some

Manuscript received September 22, 2017; final manuscript received January 2, 2018; published online March 9, 2018. Assoc. Editor: Johnson Samuel.

This material is declared a work of the U.S. Government and is not subject to copyright protection in the United States. Approved for public release; distribution is unlimited.

have integrated investigations at the macro, meso, and micro levels to simulate and assess residual stress in parts [46,47].

The newness of AM modeling poses challenges for its immediate use by AM industry. Figure 1 outlines current critical steps for addressing residual stress in metal AM parts to ultimately achieve improved AM efficiency. AM efficiency, in this case, refers to fabricating high quality AM parts with minimized time and waste. To minimize residual stress, an understanding of the stress distribution within a part is essential. While physical experiments can directly attain this knowledge, if a model can expose an array of high stresses in a projected part, designers could alter the part prior to the build, which would save time and resources. Furthermore, this understanding could lead to AM process improvements by altering AM system elements, such as heating strategies, in order to mitigate residual stress.

In these early stages of model development, effective modeling techniques require validation of the simulations; therefore, certain physical experiments should be carried out that represent a broad spectrum of variables to serve as reference data for quantifying residual stress and validating the models. Improved understanding of the residual stress state will then inform model refinements. Reference data sets require forethought and care in execution. Experimental methods, machine settings, laser paths, sensor settings and gains, and even units of measurement can affect the results. Careful experimental records are necessary to ensure appropriate comparisons are being made. Measurement uncertainty is also critical to evaluate whether any differences in comparisons are significant. More innovative models and simulations will motivate continued evolution of strategies to reduce residual stress with minimal need for future physical product affirmation.

The goal of this study is to investigate residual stress in simple powder bed fusion parts to gain a better understanding of factors influencing the stress state. The study will also generate data that can be used to help improve models and simulations. Generating fundamental reference data sets is critical for the results to be generalizable to a multitude of design configurations. The study focuses on changing structural geometry to evaluate changes in residual stress. Most prior residual stress studies have used solid, prismatic geometries. The only known residual stress study incorporating round samples focused on changing the heights of cylinders with a consistent diameter as well as their positions on the build tray [30]. Furthermore, while penetrations into parts, such as what is necessary in the hole drilling method for stress

measurement, relax stresses [1,30], to the authors' knowledge there have been no studies with samples containing an intentional hole to determine if the hole serves as a natural stress relaxer. These gaps guided the decision to design cylindrical samples with different heights and outer diameters that also include holes of varied diameters. Evaluation of the residual stress in these parts could reveal overarching trends applicable to confirming and refining multiphysics models.

## 2 Background

**2.1 Additive Manufacturing Build Process.** Powder bed fusion is an AM process during which thermal energy selectively fuses regions of a powder bed [48]. As presented in Fig. 2, pistons control the powder supply and build plate. After the recoater blade spreads a fresh layer of metal powder over the build plate, mirrors and lenses direct a laser to selectively sinter powder according to the geometry of the respective cross-sectional layer of the part as provided from a computer-aided design (CAD) model. The build plate then lowers by the thickness of one layer, and the process repeats, building the part layer by layer until it is fully fabricated.

**2.2 Residual Stress Measurement.** While literature presents many residual stress measurement methods [1], neutron diffraction, one of the more well-established methods that many studies have implemented [6,7,12,16,19,22,24,27,44], was selected for this study. This method was selected because it is robust, nondestructive, and has good resolution and accuracy. During neutron diffraction, a beam of neutrons is directed into a part, and the diffraction pattern reveals the part's lattice spacing, which can further be used to calculate residual stress. To find the lattice spacing within the part,  $d$ , Bragg's law is used

$$\lambda = 2d(\sin\theta) \quad (1)$$

where  $\lambda$  is the wavelength of the neutron beam and  $\theta$  is half of the angle of diffraction. Having also measured  $d_0$ , the reference stress-free lattice spacing, lattice strain,  $\epsilon$ , can be computed as

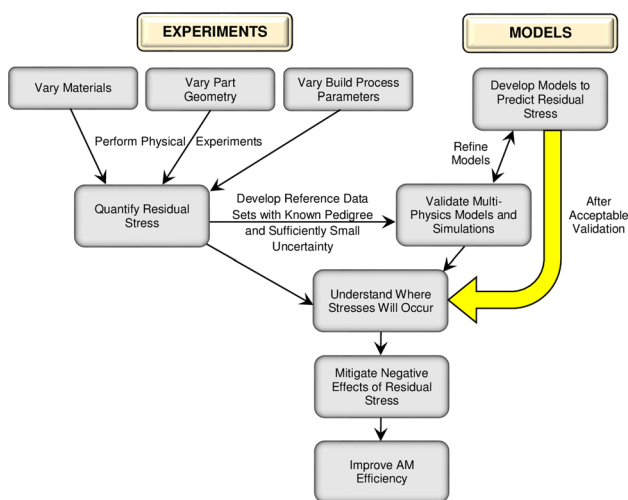


**Fig. 1** Flowchart highlighting the progression of key steps for physically measuring and modeling residual stress in metal AM parts. While experimental validation of residual stress in parts is currently necessary, model advancements will expedite the process by reducing the need for physical experiments and iterative validation.

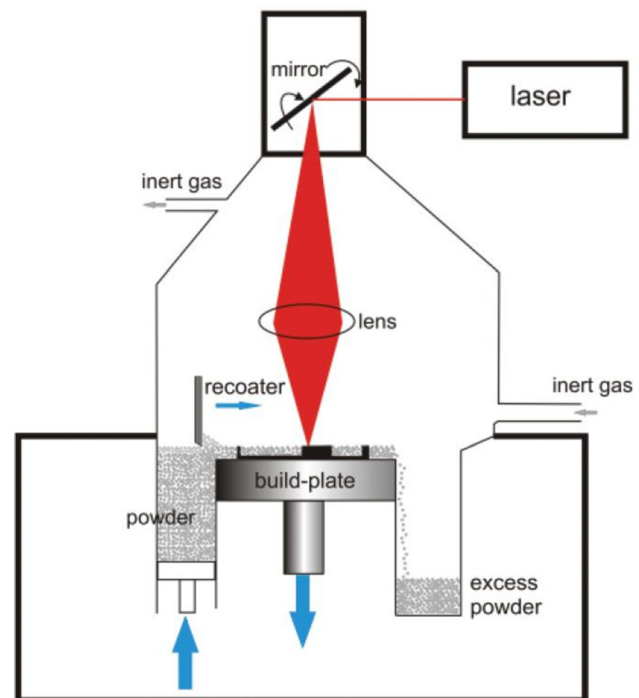


**Fig. 2** Diagram of the laser-based powder bed fusion process

**Table 1 Geometric dimensions of the samples. An inner diameter of 0 mm indicates a fully solid sample.**

Sample number	Outer diameter (mm)	Inner diameter (mm)	Height (mm)
1	6	2	10
2	6	2	25
3	6	2	40
4	6	0	10
5	6	0	25
6	6	0	40
7	12	2	10
8	12	2	25
9	12	2	40
10	12	0	10
11	12	0	25
12	12	0	40

$$\varepsilon = \frac{d - d_0}{d_0} \quad (2)$$

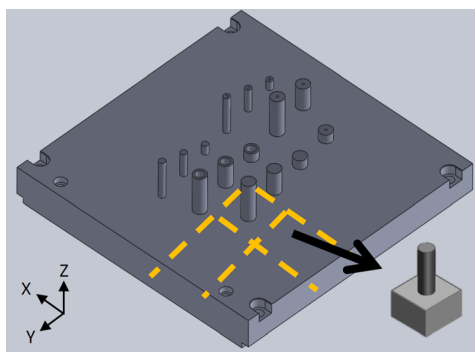
Since  $d_0$  is direction dependent, strains from Eq. (2) can be broken down into components ( $\varepsilon_x, \varepsilon_y, \varepsilon_z$ ), and Hooke's Law may be used to relate the components of strain in each direction to the three normal stress components ( $\sigma_x, \sigma_y, \sigma_z$ ) in order to achieve and analyze the 3D stress components

$$\sigma_x = \frac{E}{(1 + \nu)(1 - 2\nu)} [(1 - \nu)\varepsilon_x + \nu(\varepsilon_y + \varepsilon_z)] \quad (3)$$

$$\sigma_y = \frac{E}{(1 + \nu)(1 - 2\nu)} [(1 - \nu)\varepsilon_y + \nu(\varepsilon_x + \varepsilon_z)] \quad (4)$$

$$\sigma_z = \frac{E}{(1 + \nu)(1 - 2\nu)} [(1 - \nu)\varepsilon_z + \nu(\varepsilon_x + \varepsilon_y)] \quad (5)$$

where  $E$  is Young's modulus and  $\nu$  is Poisson's ratio. In order to determine the full 3D stress state, shear components must be considered. In many studies, shear stress is recognized to be negligible [9,19,22,31]. However, the rapid shrinkage as a layer cools above another layer could introduce shearing effects, especially when considering the diverse array of stress magnitudes that arise by changing AM processes, materials, part geometries, and build parameters. Measuring shear strain is outside of the scope of this study as it requires additional measurements along nonorthogonal directions. However, it could be useful to measure shear strains in future studies to provide additional insight into the full residual stress state of AM parts.



(a)

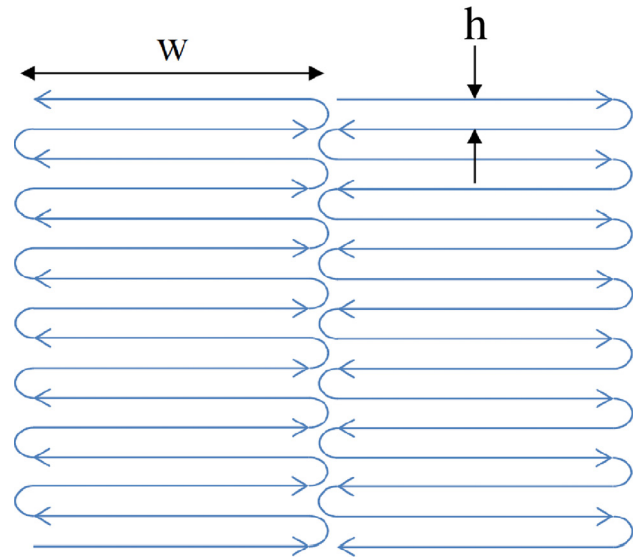


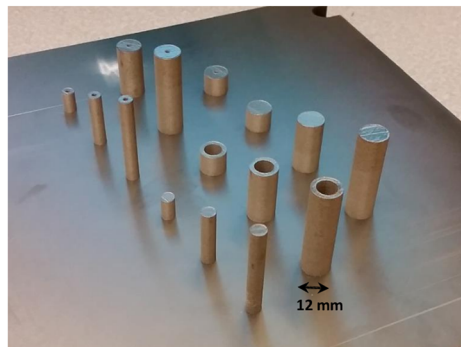
**Fig. 4 Progression of the laser beam in the internal exposure rastering pattern**

### 3 Experimental Procedures

**3.1 Sample Fabrication.** Cylindrical parts were designed with the dimensions listed in Table 1. A part had either a small or large outer diameter and was solid or had a central hole spanning along the height ( $z$ ) axis. Samples were either 10 mm, 25 mm, or 40 mm tall.

Figure 3(a) presents the CAD model of the build plate and samples, which were fabricated using Nickel Alloy 625. To arrange the build plate for the laser-based powder bed fusion process and avoid the potential for build defects, samples were centered on the build plate, heights were distributed across the build plate, and rows of samples were slightly angled relative to the build plate edges.

The build process involved scans of the precontour, the internal regions of the parts, and the postcontour. The precontour consisted of one pass at 900 mm/s using a laser power of 100 W. The internal regions of the parts received exposure with a scan speed of 800 mm/s and a laser power of 195 W. During internal exposure, a back-and-forth raster pattern created stripes as shown in Fig. 4. Each stripe had a width,  $w$ , of 4 mm and a hatch spacing,  $h$ , of 0.1 mm. Adjacent stripes overlapped by 0.1 mm, and the direction of the stripes was rotated by 67 deg for each layer to increase the likelihood of fully dense, isotropic part properties. Afterward, the



(b)

**Fig. 3 Cylindrical samples: (a) as displayed from a CAD model and (b) as built. After fabrication, the build plate was cut as shown by the dotted lines in (a) to isolate each specimen for stress measurements. The three specimens shown that have large inner diameters were not used in this study due to difficulties with measuring stress within the thin walls.**

postcontour, like the precontour, consisted of one pass at 900 mm/s with a laser power of 100 W. The parts were built with a layer thickness of 20  $\mu\text{m}$ . Figure 3(b) shows the samples fully built.

Because removing the samples from the build plate likely relaxes stresses, parts were left attached to the platform to best represent the stresses resulting from the build. To accommodate comprehensive measurement of the samples by neutron diffraction, the build plate was cut via wire electrical discharge machining such that every sample was isolated (see Fig. 3(a)). This allowed the parts to retain their full stress state while enabling

close and consistent positioning of the neutron beam in relation to each part without extraneous absorption.

**3.2 Neutron Diffraction Parameters.** Using the BT-8 residual stress diffractometer at the National Institute of Standards and Technology (NIST) Center for Neutron Research, stress measurements were taken at multiple heights spanning from two millimeters from the bottom of each part to two millimeters from the top of each part. For each height level tested, the beam scanned

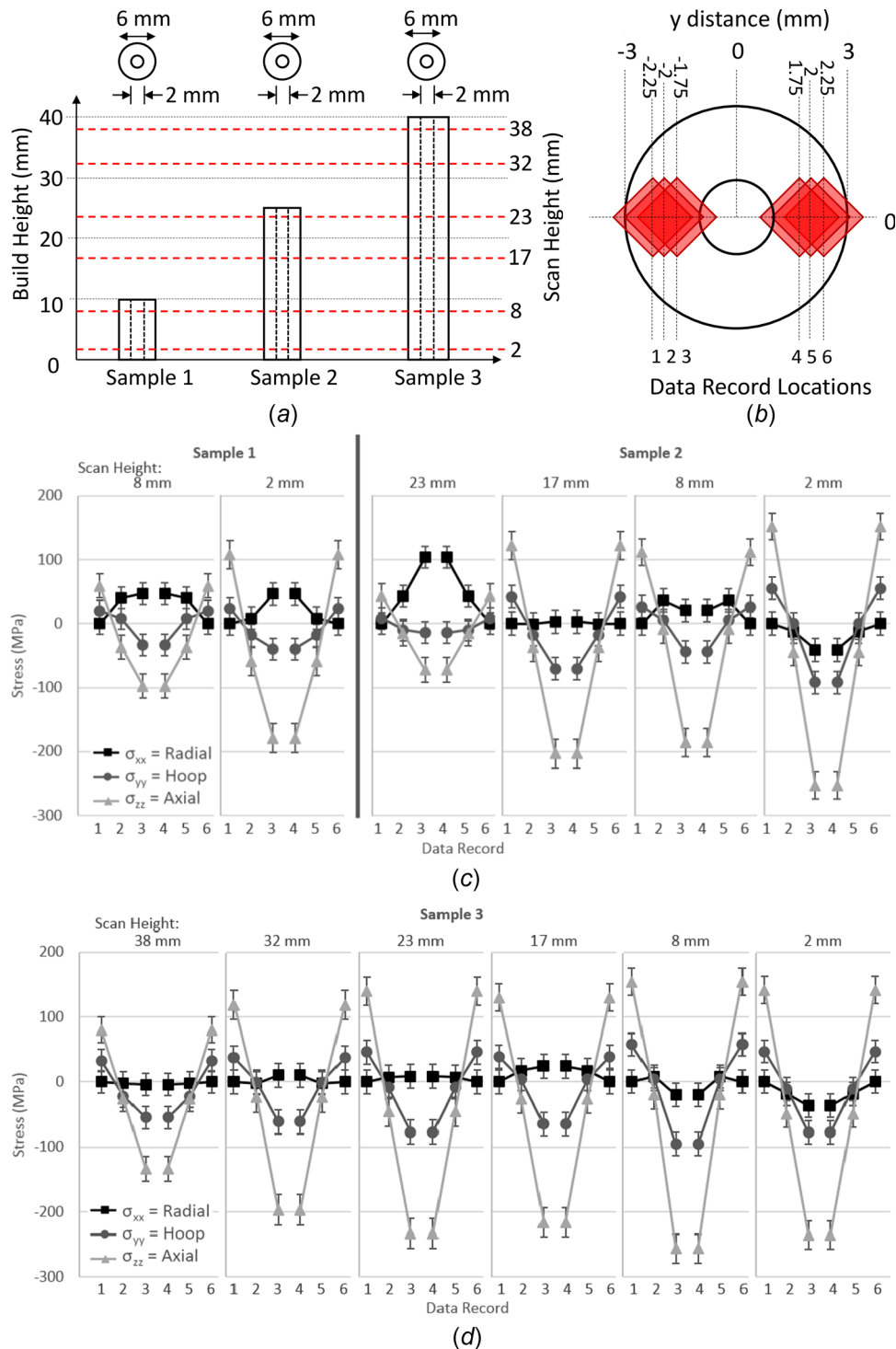


Fig. 5 Samples 1–3: (a) geometries and scan heights, (b) scan locations, (c) stresses in samples 1–2, and (d) stresses in sample 3

from  $-y$  to  $+y$  (reference Fig. 3(a)) using a neutron wavelength of 1.588 Å and a gauge volume, or measured volume, of 1.5 mm × 1.5 mm × 1.5 mm. Since Nickel Alloy 625 has a face centered cubic crystal structure, the (311) reflection plane at  $2\theta = 96.68$  deg was chosen to minimize the influence of intergranular stresses on the diffraction measurements of macroscopic stress. The stress-free lattice spacing,  $d_0$ , was calculated for each sample by utilizing near-surface measurements where the stress component normal to the surface can be presumed to be zero. In this case, radial stresses for the cylindrical samples were presumed to be zero near the surface. For this study,  $d_0$  was estimated from measurements with locations near the surface where  $\sigma_x = 0$ , or radial stress equals zero, for each sample. Each  $d_0$  estimate from the individual samples was averaged to obtain a single  $d_0$  for the corresponding sample. The  $d_0$  value varies with regard to build direction because of the intergranular strains and texture arising

from the rapid cooling of the metal. Therefore, a stress balance was also applied to further refine the measurement accuracy for both axial and hoop directions. Axial and hoop forces across each cross-sectional layer ( $y$  direction) were set to have zero net force. In addition, symmetry was applied to the measurements due to the cylindrical symmetry of the samples to further increase counting statistics. By assuming axisymmetry, certain equilibrium equations have to be satisfied. When considering cylindrical components ( $r, \theta$ , and  $z$ ), the following equations apply:

$$\frac{\delta\sigma_{rr}}{\delta r} + \frac{1}{r} \frac{\delta\sigma_{\theta r}}{\delta\theta} + \frac{\delta\sigma_{zr}}{\delta z} + \frac{\sigma_{rr} - \sigma_{\theta\theta}}{r} = 0 \quad (6)$$

$$\frac{\delta\sigma_{r\theta}}{\delta r} + \frac{1}{r} \frac{\delta\sigma_{\theta\theta}}{\delta\theta} + \frac{\delta\sigma_{z\theta}}{\delta z} + \frac{2\sigma_{r\theta}}{r} = 0 \quad (7)$$

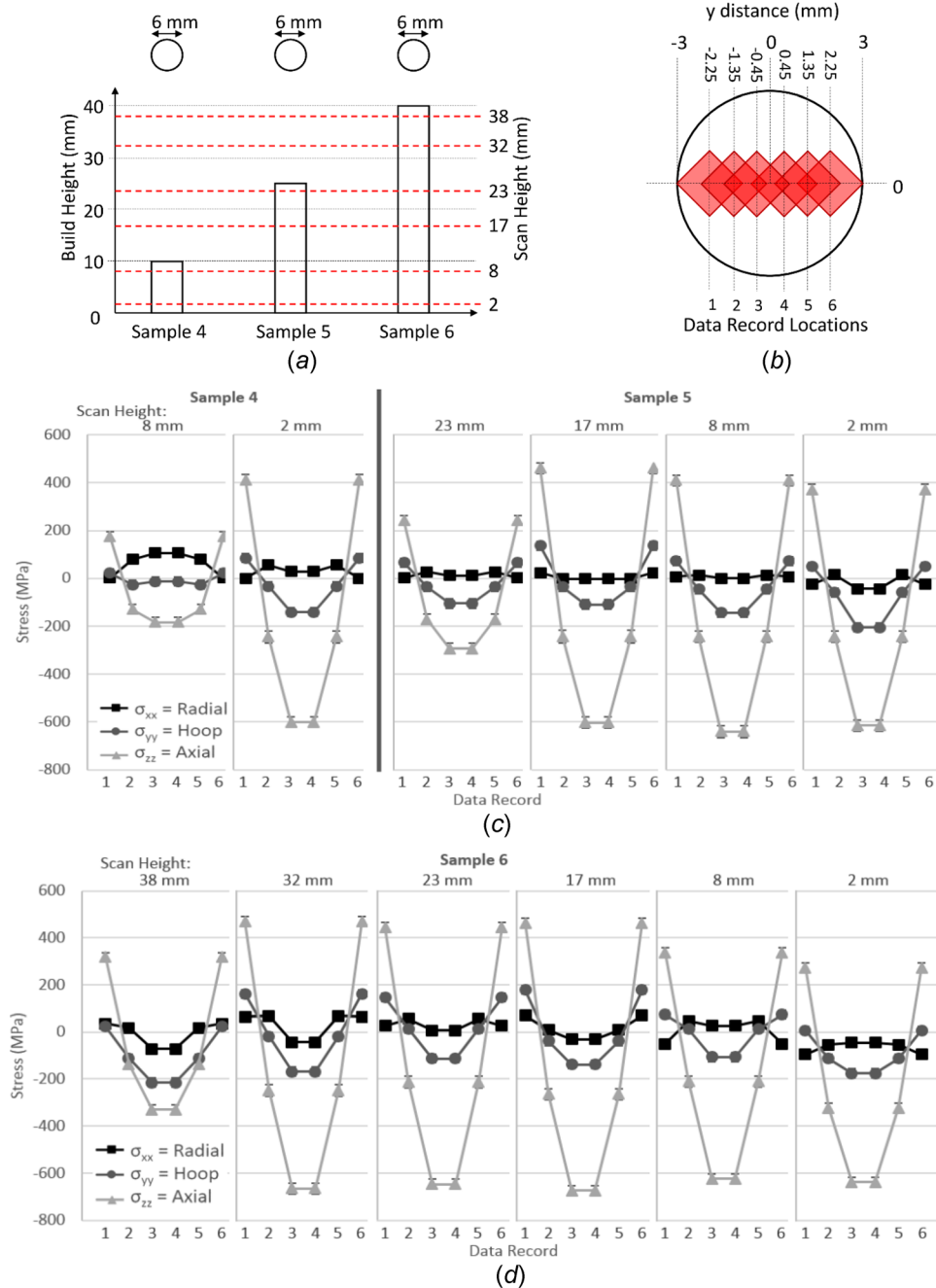


Fig. 6 Samples 4–6: (a) geometries and scan heights, (b) scan locations, (c) stresses in samples 4–5, and (d) stresses in sample 6

$$\frac{\delta\sigma_{rz}}{\delta r} + \frac{1}{r} \frac{\delta\sigma_{\theta z}}{\delta\theta} + \frac{\delta\sigma_{zz}}{\delta z} + \frac{\sigma_{rz}}{r} = 0 \quad (8)$$

#### 4 Results and Discussion

The residual stress trends for samples 1–3 are presented in Fig. 5. The error bars shown in this figure and subsequent figures represent one standard deviation of uncertainty. Figure 5(a) displays the build geometries and scan heights while Fig. 5(b) reveals the locations of each gauge volume that corresponds to a recorded data point (six locations). Because cylindrical symmetry is assumed, data points at corresponding y distances were averaged. Figure 5(c) shows radial, hoop, and axial stresses for samples 1 and 2, and Fig. 5(d) shows these stresses in sample 3.

Across the y distance, these samples show regions of high axial tension at the edges ( $\approx 125$  MPa) transitioning to high axial compression internally ( $\approx -200$  MPa). When considering changes in height within a single sample, only the topmost scan height indicates a dissimilar trend where axial tension and compression significantly decrease in magnitude. This is expected because the axial stress is zero at the surface. The exterior tension and interior compression trend is also observed in the hoop stresses but with diminished magnitudes (not more than  $\pm 100$  MPa). The radial stresses in general have the lowest magnitudes (typically  $\approx 0$  MPa) although the topmost scan of sample 2 exhibits unusually high internal radial stress. These same trends of tension transitioning to compression appear with varying magnitudes in samples 4–6 (Figs. 6(a)–6(d)), samples 7–9 (Figs. 7(a)–7(d)), and samples 10–12 (Figs. 8(a)–8(d)).

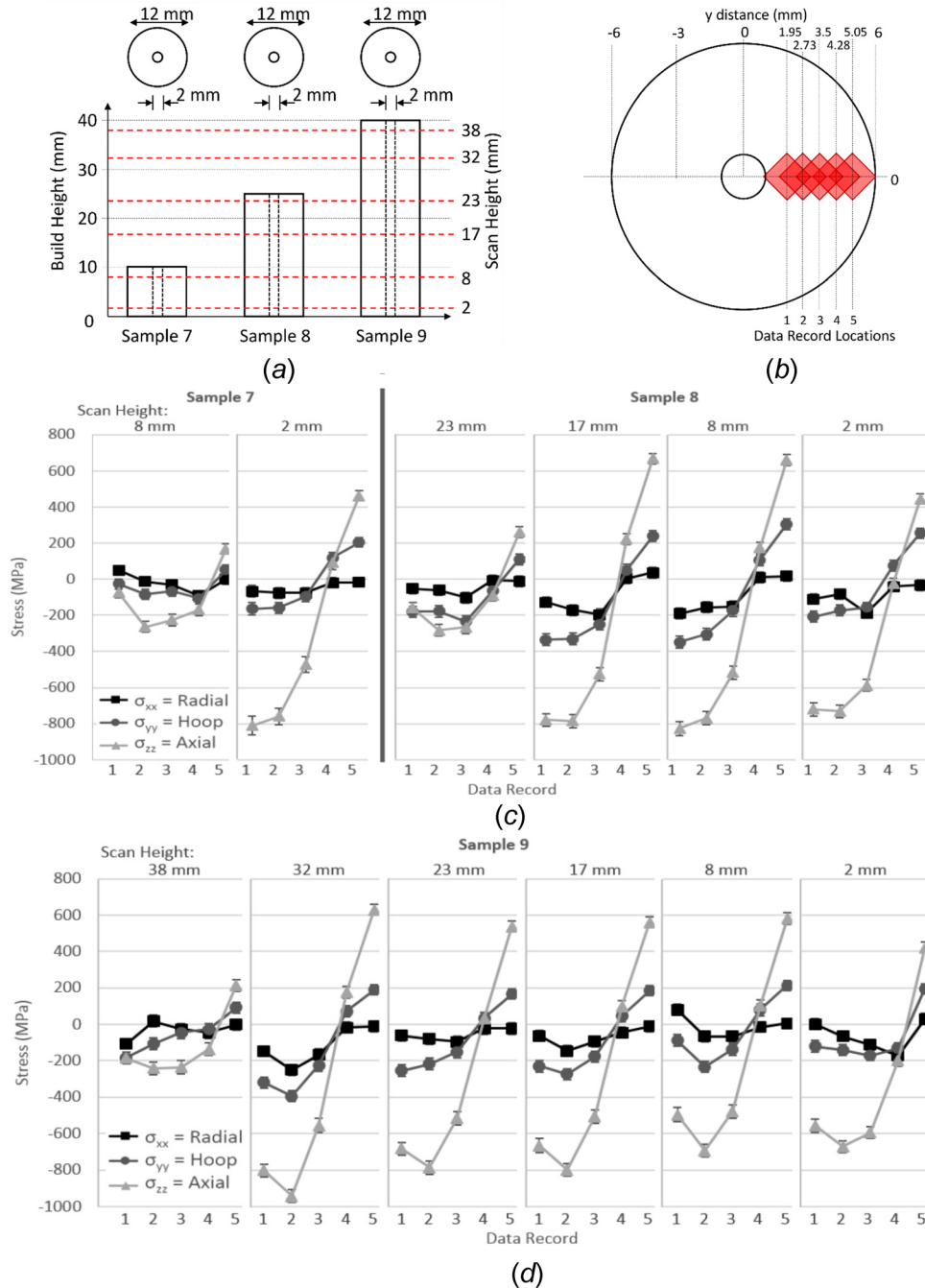


Fig. 7 Samples 7–9: (a) geometries and scan heights; (b) scan locations, (c) stresses in samples 7–8, and (d) stresses in sample 9

Samples 4–6, displayed in Fig. 6, exhibit increased tensile and compressive magnitudes for both axial stresses ( $\approx -600$  MPa to 400 MPa) and hoop stresses (not more than  $\pm 200$  MPa). This hints that the presence of a hole might serve as a natural stress reliever. However, the gauge volume selected for this study limited the ability to distinguish the stress gradients near the inner diameter. The relatively large gauge volume, as compared to the wall thickness of the cylindrical sample, causes a large averaging effect that smooths major stress gradients that may be present. This limited the ability to understand the full effects caused by the inner diameter on the stress state of the resultant sample.

Since samples 7–9, shown in Fig. 7, have larger diameters than the previous ones, scans were only conducted from the inner diameter to the outer diameter. The hoop and axial stresses here

are larger than those of the previous figures with axial stresses now ranging from  $\approx -800$  MPa to 600 MPa. These plots also indicate a slight reduction in axial compression toward the center of the parts, which was not evident in the other samples. The contour method will be used in an upcoming study to investigate this further. The contour method involves sectioning the part, which allows stresses to relax. Then, the surface contour is measured to calculate the residual stress that caused the surface deformations. The result is a 2D map showing the residual stress across the cross-sectional geometry. This will be beneficial to evaluate the stress trends near the part edges.

Measurements for samples 10–12, in Fig. 8, were spaced out to not overlap gauge volumes. They clearly show the significant drop in axial stress magnitude in the topmost scan. While the

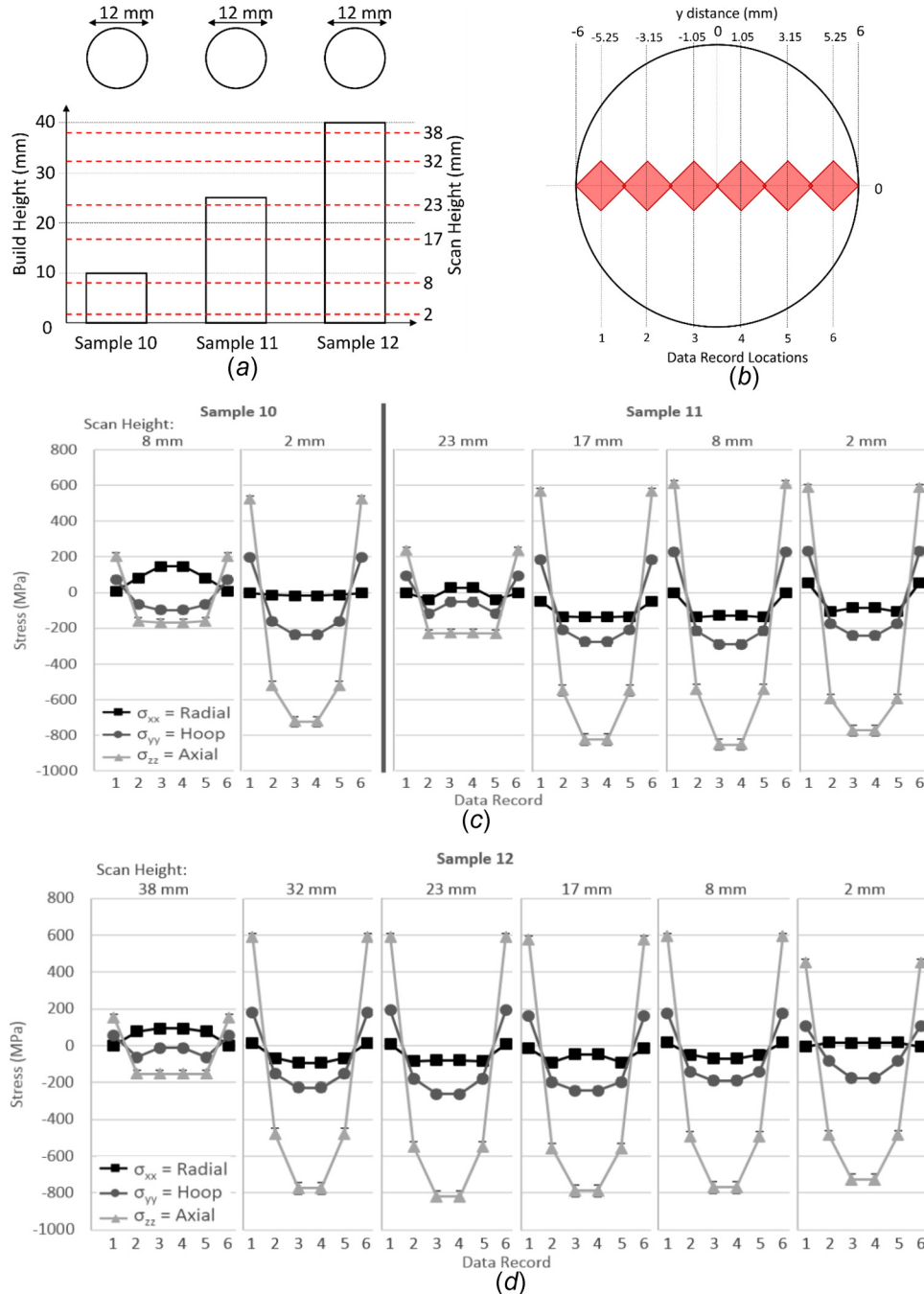


Fig. 8 Samples 10–12: (a) Geometries and scan heights, (b) scan locations, (c) stresses in samples 10–11, and (d) stresses in sample 12

middle and bottom scans hover at  $\approx -800$  MPa to 600 MPa, the topmost scan remains around  $\pm 200$  MPa. The hoop stress also indicates a slight decline at the topmost scan.

It can be noted from the plots that, in general, the radial stresses are zero at the data points closest to the part edges, which makes sense because this stress component must be zero at the free surface. The axial stresses, when integrated over the cross section, appear to result in a zero net force, which is also expected. To be consistent with expectations from the equilibrium conditions, the radial and hoop stresses should be coincident at the center of the parts. Although no measurements were taken at the exact part centers, the trends imply that these stresses would not match up. This is unexpected, and more measurements would be necessary to explain the contradiction. One potential cause could lie with the assumption of axisymmetry, which was done due to the geometry. However, if the part is not axisymmetric with regard to stress, the assumption could skew the results. A prior, similar residual stress study at NIST with square samples did find the  $x$ - and  $y$ -stress components consistent in the part center [7], further pointing to geometry being the reason for the inconsistencies.

From a report by EWI of mechanical properties for Nickel Alloy 625 manufactured via laser-based powder bed fusion, the average yield strength calculated from the provided data was 548 MPa [49]. Residual axial stresses from the present study have at times exceeded this value, which validates the need for post processing to improve the mechanical properties of final parts. Many suggest heat treatments of the part, build plate, or powder bed to reduce residual stress [2–5,9,10,13,23,25,29,34,42,45,50,51]; however, this expends time and energy. With the increase in available experimental residual stress results for a variety of AM processes, materials, and parts, more accurate models could pinpoint high-stress regions that could be redesigned to

ensure stresses remain far below the material yield strength and thus minimize the need for this post processing.

The trends from this study indicate that height does not seem to be a significant factor. Across samples with the same cross-sectional geometry, the residual stress magnitudes remain consistent (i.e., samples 1–3 ranged between  $-250$  MPa and 150 MPa for all scan heights; samples 4–6 ranged between  $-600$  MPa and 400 MPa). Because stress does not vary with build height, volume also cannot be a defining measure. An example of this can be seen when comparing samples 3 and 4. Sample 3 is taller and has a much larger volume than sample 4 but has greatly reduced stress. Cross-sectional geometry, however, seems to influence the stress magnitudes the most.

The unpredictability of stress magnitudes near the edges of the parts should also be considered. Using the experimental results, axial stress trends were developed using curve fitting. Figure 9 shows possible residual stress trends for samples 3 and 6. The plotted points are averaged from the middle heights (i.e., 8 mm, 17 mm, 23 mm, and 32 mm). The results from sample 3 appear to fit well with both a linear (Fig. 9(a)) and second-order polynomial fit (Fig. 9(b)), and both models indicate the possibility of high residual stress (up to  $\pm 800$  MPa) even in the small-diameter sample. Sample 6 is presented with a second-order polynomial fit (Fig. 9(c)), and if the stress trend were to continue, stresses up to 1200 MPa could be seen.

Similarly, Fig. 10 presents axial stress models for samples 9 and 12. Neither the linear (Fig. 10(a)) nor second-order polynomial model (Fig. 10(b)) accurately assumes the trend of the experimental data from sample 9, which could suggest a return to axial tension at the inner wall. The contour method will need to be used to validate and explore these trends further. The second-order polynomial model resembles the data of sample 12 in Fig. 10(c).

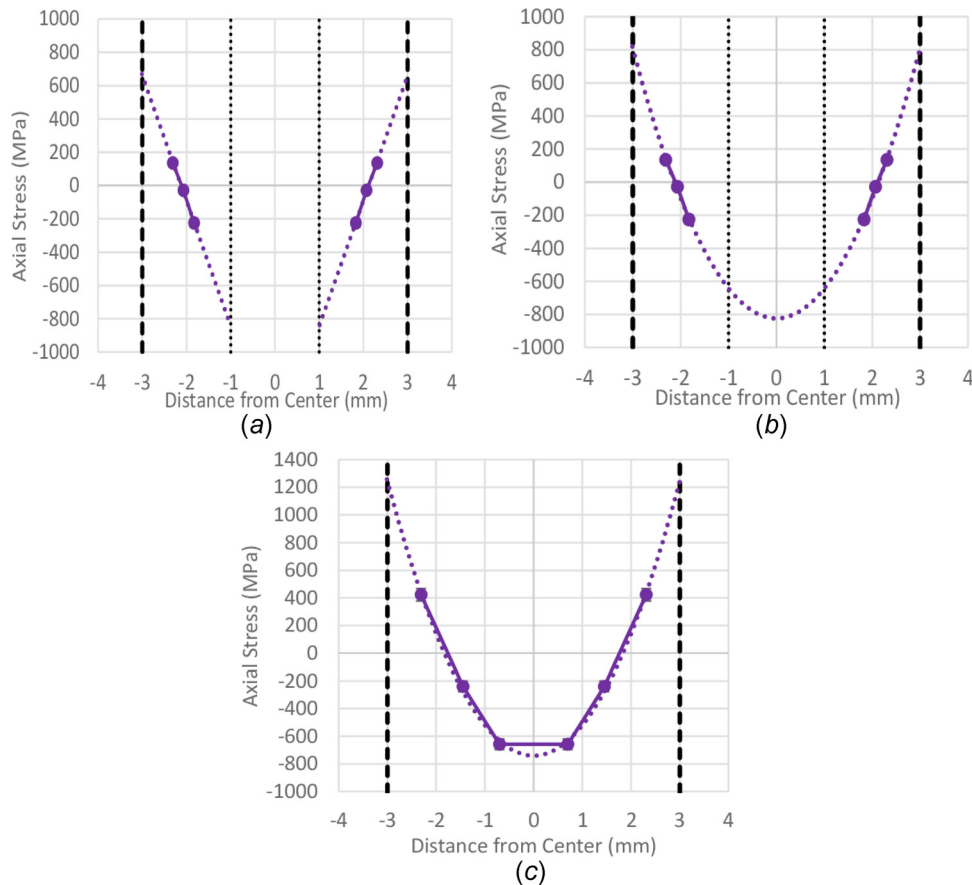


**Fig. 9** Projected axial residual stress trends for sample 3 with both (a) linear, (b) second-order polynomial fits, and (c) sample 6 with a second-order polynomial fit

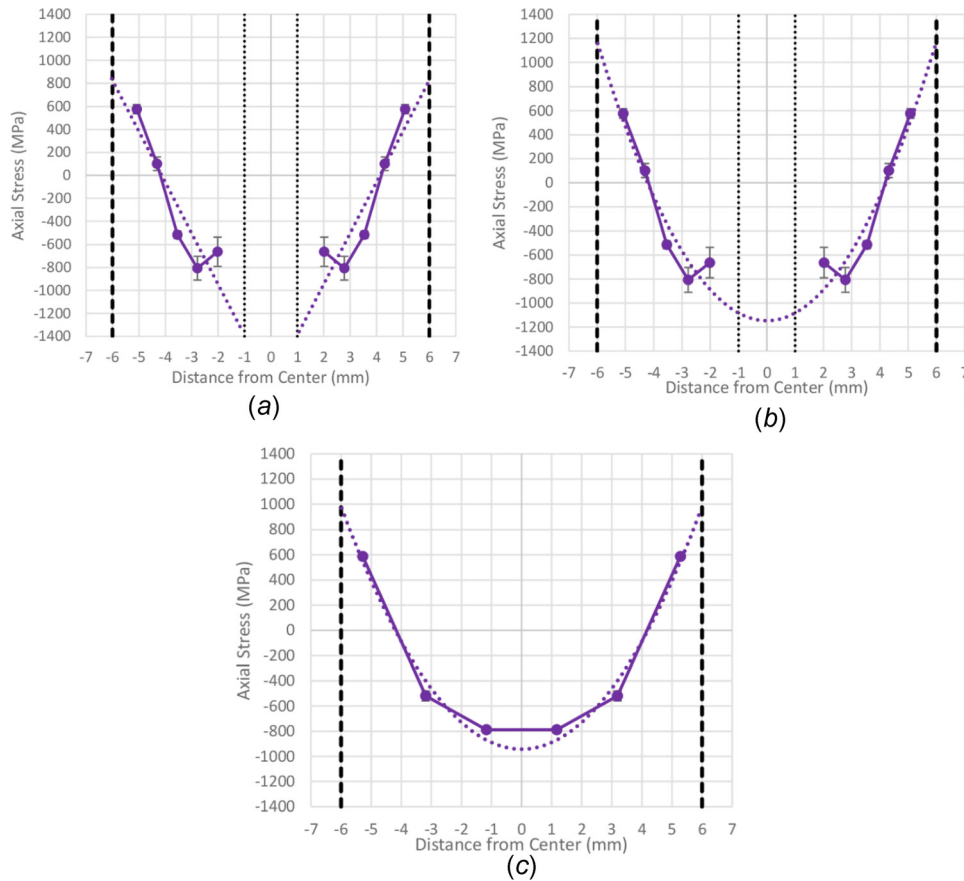


**Fig. 10 Projected axial residual stress trends for sample 9 with both (a) linear, (b) second-order polynomial fits, and (c) sample 12 with a second-order polynomial fit**

As mentioned in Sec. 1.1, temperature gradients are one of the main causes of residual stress. However, it is difficult to analyze the relationship between residual stress and the heating cycles because of the complexity of the laser-based powder bed fusion

process. Dunbar and coauthors were able to take in situ temperature and part distortion measurements for this process. They found that temperature effects deviated as builds with varying scan strategies and part distortions progressed [52]. This study further

**Table 2 Outcomes of literature most similar in nature to this study. Slight differences in material, geometry, AM process, or stress measurement method are shown to change the magnitude of stresses found.**

Author	Material/geometry	AM process	Stress measurement method	Axial stress findings across part width (maximum magnitudes given)	Compared to material yield
Rangaswamy et al. [22]	316 Stainless Steel Rectangular prisms	Direct energy deposition	Neutron diffraction	<ul style="list-style-type: none"> <li>• Largest magnitude stresses in growth direction</li> <li>• Tension exterior (<math>\approx 80</math> MPa) and compression interior (<math>\approx -380</math> MPa)</li> </ul>	Up to 50% nominal yield strength
Sochalski-Kolbus et al. [19]	Nickel Alloy 718 Rectangular prisms	Laser-based powder bed fusion	Neutron diffraction	<ul style="list-style-type: none"> <li>• Tension exterior (<math>\approx 550</math> MPa) and compression interior (<math>\approx -550</math> MPa)</li> </ul>	Well below yield strength
Wang et al. [44]	Nickel Alloy 625 Thin walls	Direct energy deposition	Neutron diffraction	<ul style="list-style-type: none"> <li>• Tension exterior (<math>\approx 300</math> MPa) and compression interior (<math>\approx -600</math> MPa)</li> </ul>	Below yield strength
Bass et al.	Nickel Alloy 625 Cylinders	Laser-based powder bed fusion	Neutron diffraction	<ul style="list-style-type: none"> <li>• Largest magnitude stresses in growth direction</li> <li>• Tension exterior (<math>\approx 600</math> MPa) and compression interior (<math>\approx -800</math> MPa)</li> </ul>	At times exceeding by $<50$ MPa in larger parts

emphasizes that every variable has the potential to cause a change in residual stress profiles as there will be a different heating cycle response for every case. While the exact results from this study will not be extendable to other materials, geometries, and build process parameters, a few trends are generalizable. For example, because the heat source always comes from above the part, the tops of parts should experience tensile stress and the bottoms should be more compressive. This is confirmed by the literature presented in Sec. 1.2.

While the trends of tensile exteriors and compressive interiors align well with literature, the literature most similar in nature to this study indicates subtle differences that cause variations in stress magnitudes (Table 2). From these comparisons, it can be concluded that a combination of factors including materials, part geometry, and build process parameters jointly determine the final outcomes of residual stress.

## 5 Conclusion

Residual stresses in cylindrical, additively manufactured Nickel Alloy 625 parts were measured by neutron diffraction to gain a better understanding of the 3D stress state in the parts. The key findings are as follows:

- Across the diameter of the parts, axial and hoop stresses were tensile on the exterior and compressive in the interior.
- Axial stresses had the greatest magnitudes, and radial stresses had the lowest magnitudes.
- At the highest scan height of every part regardless of part height, hoop and especially axial stresses lost magnitude.
- Residual stress was generally higher in parts with larger diameters, but more research is needed to verify the effects of various cross-sectional scan areas on residual stress.
- Maximum and minimum axial stress magnitudes were consistent for samples with 12 mm outer diameters. Most of the measured axial stresses for these samples were slightly above the yield stress of the material.
- For samples with small outer diameters, there appeared to be a reduction in stress with the inclusion of the hole, but this was not replicated in the samples with large outer diameters, and the contour method will be used to investigate this in future studies.
- A second-order polynomial model fits the residual stress trends found in samples that had no internal hole.

There is also the opportunity in future studies to investigate the microstructure to support efforts in identifying stress-causing factors.

Reference experimental data sets will progress future work by validating multiphysics models and simulations that predict residual stress. Increased understanding about where residual stresses occur will facilitate the development of strategies to lessen their negative effects.

## References

- [1] Withers, P. J., and Bhadeshia, H., 2001, "Residual Stress—Part 1: Measurement Techniques," *Mater. Sci. Technol.*, **17**(4), pp. 355–365.
- [2] Nickel, A. H., Barnett, D. M., and Prinz, F. B., 2001, "Thermal Stresses and Deposition Patterns in Layered Manufacturing," *Mater. Sci. Eng. A*, **317**(1–2), pp. 59–64.
- [3] Beuth, J., and Klingbeil, N., 2001, "The Role of Process Variables in Laser-Based Direct Metal Solid Freeform Fabrication," *JOM*, **53**(9), pp. 36–39.
- [4] Mercelis, P., and Kruth, J.-P., 2006, "Residual Stresses in Selective Laser Sintering and Selective Laser Melting," *Rapid Prototyping J.*, **12**(5), pp. 254–265.
- [5] Vasinonta, A., Beuth, J. L., and Griffith, M., 2007, "Process Maps for Predicting Residual Stress and Melt Pool Size in the Laser-Based Fabrication of Thin-Walled Structures," *ASME J. Manuf. Sci. Eng.*, **129**(1), pp. 101–109.
- [6] Wu, A. S., Brown, D. W., Kumar, M., Gallegos, G. F., and King, W. E., 2014, "An Experimental Investigation Into Additive Manufacturing-Induced Residual Stresses in 316L Stainless Steel," *Metall. Mater. Trans. A*, **45**(13), pp. 6260–6270.
- [7] Gnäupel-Herold, T., Slotwinski, J., and Moylan, S., 2014, "Neutron Measurements of Stresses in a Test Artifact Produced by Laser-Based Additive Manufacturing," *AIP Conf. Proc.*, **1205**, pp. 1205–1212.
- [8] Thijs, L., Verhaeghe, F., Craeghs, T., Humbeeck, J. V., and Kruth, J.-P., 2010, "A Study of the Microstructural Evolution During Selective Laser Melting of Ti-6Al-4V," *Acta Mater.*, **58**(9), pp. 3303–3312.
- [9] Mishurova, T., Cabeza, S., Artzt, K., Haubrich, J., Klaus, M., Genzel, C., Requena, G., and Bruno, G., 2017, "An Assessment of Subsurface Residual Stress Analysis in SLM Ti-6Al-4V," *Materials*, **10**(4), p. 348.
- [10] Gusarov, A. V., Pavlov, M., and Smurov, I., 2011, "Residual Stresses at Laser Surface Remelting and Additive Manufacturing," *Phys. Proc.*, **12**(Pt. A), pp. 248–254.
- [11] Forooghi, E., and Kovacevic, R., 2010, "Effect of Path Planning on the Laser Powder Deposition Process: Thermal and Structural Evaluation," *Int. J. Adv. Manuf. Technol.*, **51**(5–8), pp. 659–669.
- [12] Zaeh, M. F., and Branner, G., 2010, "Investigations on Residual Stresses and Deformations in Selective Laser Melting," *Prod. Eng.*, **4**(1), pp. 35–45.
- [13] Mughal, M. P., Fawad, H., and Mufti, R., 2006, "Finite Element Prediction of Thermal Stresses and Deformations in Layered Manufacturing of Metallic Parts," *Acta Mech.*, **183**(1–2), pp. 61–79.
- [14] Denlinger, E. R., Heigel, J. C., Michaleris, P., and Palmer, T. A., 2015, "Effect of Inter-Layer Dwell Time on Distortion and Residual Stress in Additive Manufacturing of Titanium and Nickel Alloys," *J. Mater. Process. Technol.*, **215**, pp. 123–131.
- [15] Somashekara, M. A., Naveenkumar, M., Kumar, A., Viswanath, C., and Simhambhatla, S., 2016, "Investigations Into Effect of Weld-Deposition Pattern on Residual Stress Evolution for Metallic Additive Manufacturing," *Int. J. Adv. Manuf. Technol.*, **90**(5–8), pp. 2009–2025.
- [16] Brown, D. W., Bernardin, J. D., Carpenter, J. S., Clausen, B., Spemjak, D., and Thompson, J. M., 2016, "Neutron Diffraction Measurements of Residual Stress in Additively Manufactured Stainless Steel," *Mater. Sci. Eng. A*, **678**, pp. 291–298.
- [17] Parry, L., Ashcroft, I., Bracket, D., and Wildman, R. D., 2014, "Investigation of Residual Stresses in Selective Laser Melting," *Key Eng. Mater.*, **627**, pp. 129–132.
- [18] van Belle, L., Vansteenkiste, G., and Boyer, J. C., 2013, "Investigation of Residual Stresses Induced During the Selective Laser Melting Process," *Key Eng. Mater.*, **554–557**, pp. 1828–1834.
- [19] Sochalski-Kolbus, L. M., Payzant, E. A., Cornwell, P. A., Watkins, T. R., Babu, S. S., Dehoff, R. R., Lorenz, M., Ovchinnikova, O., and Duty, C., 2015, "Comparison of Residual Stresses in Inconel 718 Simple Parts Made by Electron Beam Melting and Direct Laser Metal Sintering," *Metall. Mater. Trans. A*, **46**(3), pp. 1419–1432.
- [20] Cottam, R., Wang, J., and Luzin, V., 2014, "Characterization of Microstructure and Residual Stress in a 3D H13 Tool Steel Component Produced by Additive Manufacturing," *J. Mater. Res.*, **29**(17), pp. 1978–1986.
- [21] Withers, P. J., and Bhadeshia, H., 2001, "Residual Stress. Part 2—Nature and Origins," *Mater. Sci. Technol.*, **17**(4), pp. 366–375.
- [22] Rangaswamy, P., Griffith, M. L., Prime, M. B., Holden, T. M., Rogge, R. B., Edwards, J. M., and Sebring, R. J., 2005, "Residual Stresses in LENS<sup>®</sup> Components Using Neutron Diffraction and Contour Method," *Mater. Sci. Eng. A*, **399**(1–2), pp. 72–83.
- [23] Vrancken, B., Thijs, L., Kruth, J.-P., and Van Humbeeck, J., 2012, "Heat Treatment of Ti6Al4V Produced by Selective Laser Melting: Microstructure and Mechanical Properties," *J. Alloys Compd.*, **541**, pp. 177–185.
- [24] Moat, R. J., Pinkerton, A. J., Li, L., Withers, P. J., and Preuss, M., 2011, "Residual Stresses in Laser Direct Metal Deposited Waspaloy," *Mater. Sci. Eng. A*, **528**(6), pp. 2288–2298.
- [25] Simonelli, M., Tse, Y. Y., and Tuck, C., 2014, "Effect of the Build Orientation on the Mechanical Properties and Fracture Modes of SLM Ti-6Al-4V," *Mater. Sci. Eng. A*, **616**, pp. 1–11.
- [26] Song, B., Dong, S., Liu, Q., Liao, H., and Coddet, C., 2014, "Vacuum Heat Treatment of Iron Parts Produced by Selective Laser Melting: Microstructure, Residual Stress and Tensile Behavior," *Mater. Des.*, **54**, pp. 727–733.
- [27] Hoye, N., Li, H. J., Cuiuri, D., and Paradowska, A. M., 2014, "Measurement of Residual Stresses in Titanium Aerospace Components Formed Via Additive Manufacturing," *Mater. Sci. Forum*, **777**, pp. 124–129.
- [28] Vrancken, B., Cain, V., Knutsen, R., and Van Humbeeck, J., 2014, "Residual Stress Via the Contour Method in Compact Tension Specimens Produced Via Selective Laser Melting," *Scr. Mater.*, **87**, pp. 29–32.
- [29] Shiomi, M., Osakada, K., Nakamura, K., Yamashita, T., and Abe, F., 2004, "Residual Stress Within Metallic Model Made by Selective Laser Melting Process," *CIRP Ann.-Manuf. Technol.*, **53**(1), pp. 195–198.
- [30] Casavola, C., Campanelli, S. L., and Pappalettere, C., 2009, "Preliminary Investigation on Distribution of Residual Stress Generated by the Selective Laser Melting Process," *J. Strain Anal. Eng. Des.*, **44**(1), pp. 93–104.
- [31] Vrancken, B., Wauthlé, R., Kruth, J.-P., and Van Humbeeck, J., 2013, "Study of the Influence of Material Properties on Residual Stress in Selective Laser Melting," *Solid Freeform Fabrication Symposium (SFF)*, Austin, TX, Aug. 12–14, p. 393.
- [32] Szost, B. A., Terzi, S., Martina, F., Boisselier, D., Prytuliak, A., Pirling, T., Hofmann, M., and Jarvis, D. J., 2016, "A Comparative Study of Additive Manufacturing Techniques: Residual Stress and Microstructural Analysis of CLAD and WAAM Printed Ti-6Al-4V Components," *Mater. Des.*, **89**, pp. 559–567.
- [33] Luzin, V., and Hoye, N., 2017, "Stress in Thin Wall Structures Made by Layer Additive Manufacturing," *Mater. Res. Proc.*, **2**, pp. 497–502.
- [34] Kruth, J.-P., Deckers, J., Yasa, E., and Wauthle, R., 2012, "Assessing and Comparing Influencing Factors of Residual Stresses in Selective Laser Melting Using a Novel Analysis Method," *Proc. Inst. Mech. Eng., Part B*, **226**(6), pp. 980–991.

- [35] Gu, D., and He, B., 2016, "Finite Element Simulation and Experimental Investigation of Residual Stresses in Selective Laser Melted Ti-Ni Shape Memory Alloy," *Comput. Mater. Sci.*, **117**, pp. 221–232.
- [36] Hodge, N. E., Ferencz, R. M., and Vignes, R. M., 2016, "Experimental Comparison of Residual Stresses for a Thermomechanical Model for the Simulation of Selective Laser Melting," *Addit. Manuf.*, **12**(Pt. B), pp. 159–168.
- [37] Fergani, O., Berto, F., Welo, T., and Liang, S. Y., 2016, "Analytical Modelling of Residual Stress in Additive Manufacturing," *Fatigue Fract. Eng. Mater. Struct.*, **40**(6), pp. 971–978.
- [38] Mukherjee, T., Zhang, W., and DebRoy, T., 2017, "An Improved Prediction of Residual Stresses and Distortion in Additive Manufacturing," *Comput. Mater. Sci.*, **126**, pp. 360–372.
- [39] Ding, J., Colegrove, P., Mehnen, J., Williams, S., Wang, F., and Almeida, P. S., 2014, "A Computationally Efficient Finite Element Model of Wire and Arc Additive Manufacture," *Int. J. Adv. Manuf. Technol.*, **70**(1–4), pp. 227–236.
- [40] Hodge, N. E., Ferencz, R. M., and Solberg, J. M., 2014, "Implementation of a Thermomechanical Model for the Simulation of Selective Laser Melting," *Comput. Mech.*, **54**(1), pp. 33–51.
- [41] Schilp, J., Seidel, C., Krauss, H., and Weirather, J., 2015, "Investigations on Temperature Fields During laser beam Melting by Means of Process Monitoring and Multiscale Process Modelling," *Adv. Mech. Eng.*, **6**, p. 217584.
- [42] Bai, X., Zhang, H., and Wang, G., 2014, "Modeling of the Moving Induction Heating Used as Secondary Heat Source in Weld-Based Additive Manufacturing," *Int. J. Adv. Manuf. Technol.*, **77**(1–4), pp. 717–727.
- [43] Zohdi, T. I., 2015, "Modeling and Simulation of Cooling-Induced Residual Stresses in Heated Particulate Mixture Depositions in Additive Manufacturing," *Comput. Mech.*, **56**(4), pp. 613–630.
- [44] Wang, Z., Denlinger, E., Michaleris, P., Stoica, A. D., Ma, D., and Beese, A. M., 2017, "Residual Stress Mapping in Inconel 625 Fabricated Through Additive Manufacturing: Method for Neutron Diffraction Measurements to Validate Thermomechanical Model Predictions," *Mater. Des.*, **113**, pp. 169–177.
- [45] Masoomi, M., Thompson, S. M., and Shamsaei, N., 2017, "Laser Powder Bed Fusion of Ti-6Al-4V Parts: Thermal Modeling and Mechanical Implications," *Int. J. Mach. Tools Manuf.*, **118–119**, pp. 73–90.
- [46] Li, C., Fu, C. H., Guo, Y. B., and Fang, F. Z., 2016, "A Multiscale Modeling Approach for Fast Prediction of Part Distortion in Selective Laser Melting," *J. Mater. Process. Technol.*, **229**, pp. 703–712.
- [47] Liou, F., Newkirk, J., Fan, Z., Sparks, T., Chen, X., Fletcher, K., Zhang, J., Zhang, Y., Kumar, K. S., and Karnati, S., 2015, "Multiscale and Multiphysics Modeling of Additive Manufacturing of Advanced Materials," NASA Langley Research Center, Hampton, VA, Technical Report No. [NASA/CR-2015-218691](#).
- [48] ASTM International, 2016, "Standard Terminology for Additive Manufacturing—General Principles-Terminology," ASTM International, West Conshohocken, PA, Standard No. [ISO/ASTM52900-1](#).
- [49] Kelly, S., 2014, "Volume 1: Development of Mechanical Property Data for Laser Powder Bed Fusion Additive Manufacturing of Nickel Alloy 625," EWI, Columbus, OH, Technical Report No. [53776GTH](#).
- [50] Idell, Y., Levine, L. E., Allen, A. J., Zhang, F., Campbell, C. E., Olson, G. B., Gong, J., Snyder, D. R., and Deutchman, H. Z., 2016, "Unexpected  $\delta$ -Phase Formation in Additive-Manufactured Ni-Based Superalloy," *JOM*, **68**(3), pp. 950–959.
- [51] Ali, H., Ma, L., Ghadbeigi, H., and Mumtaz, K., 2017, "In-Situ Residual Stress Reduction, Martensitic Decomposition and Mechanical Properties Enhancement Through High Temperature Powder Bed Pre-Heating of Selective Laser Melted Ti6Al4V," *Mater. Sci. Eng. A*, **695**, pp. 211–220.
- [52] Dunbar, A. J., Denlinger, E. R., Heigel, J., Michaleris, P., Guerrier, P., Martukanitz, R., and Simpson, T. W., 2016, "Development of Experimental Method for in Situ Distortion and Temperature Measurements During the Laser Powder Bed Fusion Additive Manufacturing Process," *Addit. Manuf.*, **12**(Pt. A), pp. 25–30.